

Observation of a propagating slow magnetoacoustic wave in a coronal plasma fan with SDO/AIA and SoHO/EUI

Rebecca L. Meadowcroft,¹★ Sihui Zhong¹,¹ Dmitrii Y. Kolotkov^{1,2} and Valery M. Nakariakov^{1,3}★

¹Centre for Fusion, Space and Astrophysics, Physics Department, University of Warwick, Coventry CV4 7AL, UK

²Engineering Research Institute ‘Ventspils International Radio Astronomy Centre (VIRAC)’, Ventspils University of Applied Sciences, Ventspils, LV-3601, Latvia

³Centro de Investigacion en Astronomía, Universidad Bernardo O’Higgins, Avenida Viel 1497, Santiago, Chile

Accepted 2023 November 8. Received 2023 November 8; in original form 2023 July 24

ABSTRACT

Simultaneous observations of a propagating disturbance of EUV intensity, with SDO/AIA at 171 Å and SoHO/EUI-HRIEUV at 174 Å, are investigated. The disturbance moves outwards along a plasma fan structure in active region AR 12941 on February 7th 2022, at 12:45–14:15 UT. The spacecraft line-of-sight separation is 19°. The variation of the EUV intensity resembles an almost harmonic wave with an oscillation period of $2.7^{+0.1}_{-0.2}$ and $2.6^{+0.1}_{-0.1}$ min for AIA and HRIEUV, respectively. Over 30 oscillation cycles are detected. The wave originated at the footpoint of the fan, anchored in a sunspot. The projected phase speeds are 60.5 ± 5.2 and 74.4 ± 6.2 km s⁻¹ in the AIA and HRIEUV data, respectively, determined by the cross-correlation technique. The observed parameters of the propagating EUV disturbance suggest its interpretation as a slow magnetoacoustic wave. Observations with AIA show that the wave decays with height, with a calculated *e*-folding length of $6.9^{+1.3}_{-0.8}$ Mm. In contrast, in the HRIEUV data, the propagating EUV disturbance is also seen much higher, with the *e*-folding length of $12.8^{+1.1}_{-1.7}$ Mm. This observation demonstrates, for the first time, that the apparent spatial damping of propagating slow waves depends on the observational instrument. Moreover, our work shows that the study of slow waves can be advanced with the use of HRIEUV, and multiple instruments with non-parallel lines of sight.

Key words: waves – Sun: corona – Sun: oscillations.

1 INTRODUCTION

Slow magnetoacoustic waves are among the most studied and frequently detected wave motions in the corona of the Sun (e.g. Nakariakov & Kolotkov 2020). The waves appear in both propagating and standing forms, as well as in a currently debated sloshing form (see Banerjee et al. 2021; Wang et al. 2021, for recent comprehensive reviews). The first direct detections of slow magnetoacoustic waves in the solar corona were reported by Berghmans & Clette (1999) and DeForest & Gurman (1998) in coronal plasma fans and polar plumes, respectively, with the space-borne imaging telescope EIT on the SOHO spacecraft. Later on, a number of propagating slow waves were observed with TRACE (De Moortel, Ireland & Walsh 2000; De Moortel et al. 2002a) and SDO/AIA instruments (Krishna Prasad, Banerjee & Singh 2012a). Propagating coronal slow waves have also been detected as approximately in-phase variations of the Doppler shift and intensity oscillations of coronal spectral lines (Wang et al. 2009a; Wang, Ofman & Davila 2009b). In addition, quasi-periodic variations in the polarized brightness of the white light in the polar coronal holes could also be associated with slow waves (Ofman et al. 1997). Propagating slow waves are characterized by a relative

perturbation of the EUV intensity less than several per cent (e.g. De Moortel 2006; de Moortel 2009). Typical oscillation periods range from a few to several minutes, while sometimes longer oscillation periods are observed too (e.g. Krishna Prasad et al. 2012b; Mandal, Krishna Prasad & Banerjee 2018). The waves show a very high degree of monochromaticity. Estimated phase speeds are from several tens to over a hundred km s⁻¹, which is comparable to the sound speed estimated by the temperature of the emitting plasma. The phase speed was found to increase with the temperature, following the square-root dependence predicted for slow-mode magnetoacoustic waves (Uritsky et al. 2013). That finding generalized an earlier result obtained for the loops rooted in sunspots (Kiddie et al. 2012). The waves are seen to propagate from the low corona outward, along the expected direction of the magnetic field. The loops hosting the slow waves are usually stable, quiescent loops (De Moortel et al. 2002b), without any visible activity in the form of jets or microflares. In spectral observations, the upward propagating slow waves inherently have a bias towards enhancement of the emission in the blue wing of the emission line due to the in-phase behaviour of velocity and density perturbations, which should not be confused with upflows (Verwichte et al. 2010). Propagating slow waves detected in plumes have similar properties (e.g. Nakariakov 2006; Banerjee et al. 2021).

Propagating slow waves experience a very rapid decay with height. Typical apparent damping distances are about 10 Mm, e.g. 8.9 ± 4.4 Mm as estimated in De Moortel et al. (2002a). In some works, the

* E-mail: rebecca.meadowcroft@warwick.ac.uk (RLM);
v.nakariakov@warwick.ac.uk

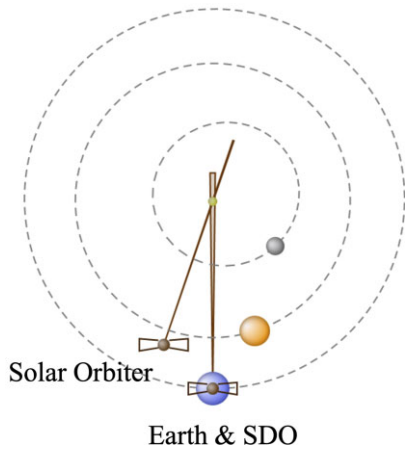


Figure 1. The location of SDO and SoLO spacecraft in relation to the Sun (centre) and Mercury, Venus, and the Earth in the ecliptic plane on the 7th of February 2022 between 12:45 and 14:15 UT. The angular separation between SDO and SoLO is 19° . This is a screenshot taken using the propagation tool (<http://propagationtool.cdpp.eu/>).

damping distance is larger, e.g. over $20 R_\odot$ (Marsh, De Moortel & Walsh 2011). Krishna Prasad et al. (2012b); Krishna Prasad, Banerjee & Van Doorselaere (2014) analysed the empirical dependence of damping lengths on the oscillation periods. The damping lengths can either increase or decrease with the increase in the period, which is definitely inconsistent with the available theory. Observations do not indicate any apparent decrease in the damping length with the temperature either (Krishna Prasad, Jess & Van Doorselaere 2019), which is also a puzzle. In agreement with this empirical result, Mandal, Krishna Prasad & Banerjee (2018) established an inverse power-law dependence of the damping length on the periodicity of slow waves observed in plumes and the interplume medium. On the other hand, the apparent rapid decay of upwardly propagating slow waves poses a question about the nature of periodic compressive perturbations detected at much larger heights, for example, the 9-min oscillations detected at $1.9 R_\odot$ by Ofman et al. (1997), and 7–8 min oscillations detected between 1.5 and $2.2 R_\odot$ by Morgan, Habbal & Li (2004).

The first two-spacecraft observation of propagating coronal slow waves was reported in Robbrecht et al. (2001), in the 171 \AA channel of TRACE and the 195 \AA channel of EIT. The projected phase speeds varied between 65 and 150 km s^{-1} for both the instruments. The simultaneous detection of slow waves in two different observational passbands of TRACE, corresponding to two different temperatures, revealed a decrease in the cross-correlation coefficient of the oscillatory signals with height (King et al. 2003). This effect was attributed to the phase mixing of wave motions propagating along the same path but along plasma threads of different temperatures. Marsh et al. (2003) reported the simultaneous detection of EUV intensity disturbances with the period of about 200 – 500 s and projected speed of 50 – 195 km s^{-1} with TRACE and the Coronal Diagnostic Spectrometer (CDS) on SOHO. A similar periodicity was detected in the variation of chromospheric and transition region emission lines. Marsh, Walsh & Plunkett (2009) performed the first quasi-stereoscopic observation of a slow coronal wave process from two non-parallel vantage points with twin STEREO A and B spacecrafts. The wave vector was inferred to have an inclination of $37^\circ \pm 6^\circ$ to the local normal to the solar surface. The true phase speed was about 132 km s^{-1} . Similar wave motions were detected by Stenborg et al.

(2011), while the study was restricted to the use of a single viewpoint only.

Slow waves propagating along coronal loops are modelled as slow magnetoacoustic waves propagating almost along the magnetic field. The simplest model of the slow wave dynamics is the infinite field model corresponding to the zero- β case, in which the description is reduced to a set of 1D acoustic equations. In that model, the phase speed of slow waves is the sound speed. More advanced models are the first-order and second-order thin flux tube approximations (Roberts & Webb 1978; Zhugzhda 1996), which allow for the finite- β effects. In particular, it is the geometric dispersion caused by the effects of the external medium and the finite cross-section. The phase speed varies between the sound speed and a so-called tube (or cusp) speed, which is essentially subsonic. Employing the infinite field approximation, Nakariakov et al. (2000) derived a weakly non-linear evolutionary equation that governs the amplitude and shape of a wave excited at a footpoint at various locations along the loop. The model accounted for the stratification and a semicircular shape of the waveguiding loop. It was shown that for certain combinations of the model parameters, the rapid damping could be caused by non-linear steepening. The model was further developed by accounting for the effect of a non-zero plane inclination angle and the offset of the circular loop centre from the baseline (Tsiklauri & Nakariakov 2001).

The rapid damping could also have been attributed to the enhanced damping by parallel thermal conduction (e.g. De Moortel & Hood 2003), while the classical values of the thermal conduction coefficient are insufficient to explain the observed wave damping (e.g. Marsh, De Moortel & Walsh 2011). That model has been generalized by accounting for the stratification, non-uniformity of the cross-section of the waveguiding magnetic flux tube, optically thin radiation and compressive viscosity (De Moortel & Hood 2004; Owen, De Moortel & Hood 2009). Implementing anisotropic thermal conduction as the damping mechanism, Mandal et al. (2016) performed forward modelling of the observational manifestation of slow waves in the EUV band. Recently, it was suggested that the slow wave damping could be caused by the back reaction of the wave-induced misbalance of the coronal heating and cooling processes (Kolotkov, Nakariakov & Zavershinskii 2019). For standing slow waves, the scaling of observed damping times with the oscillation periods was found to be generally consistent with this scenario (Kolotkov & Nakariakov 2022; Arregui, Kolotkov & Nakariakov 2023). The dependence of phase shifts of density and temperature perturbations relative to the velocity and their dependence on the equilibrium parameters of the plasma were studied in Van Doorselaere et al. (2011); Prasad, Srivastava & Wang (2021). Kolotkov (2022) generalized these studies for the regime of standing slow waves with full non-adiabaticity, i.e. without applying restrictions on the efficiency of the thermal conduction process. Propagating coronal slow waves could be excited by the leakage of chromospheric oscillations (Botha et al. 2011), with the oscillation period determined by the chromospheric resonant cavity.

Propagating slow waves is a promising tool for the seismological diagnostics of the corona. In the low- β plasma, slow waves propagate almost along the magnetic field, allowing for tracing its 3D geometry (Morgan & Hutton 2018). Different propagation speeds in two distinct temperature channels were interpreted as seismological evidence of the multistranded and multithermal nature of the loop (King et al. 2003; Krishna Prasad et al. 2017). Recently, coronal slow waves were shown to carry useful information about the coronal heating function (e.g. Reale et al. 2019; Kolotkov, Duckenfield & Nakariakov 2020; Kolotkov, Nakariakov & Fihosy 2023). Van Doorselaere et al.

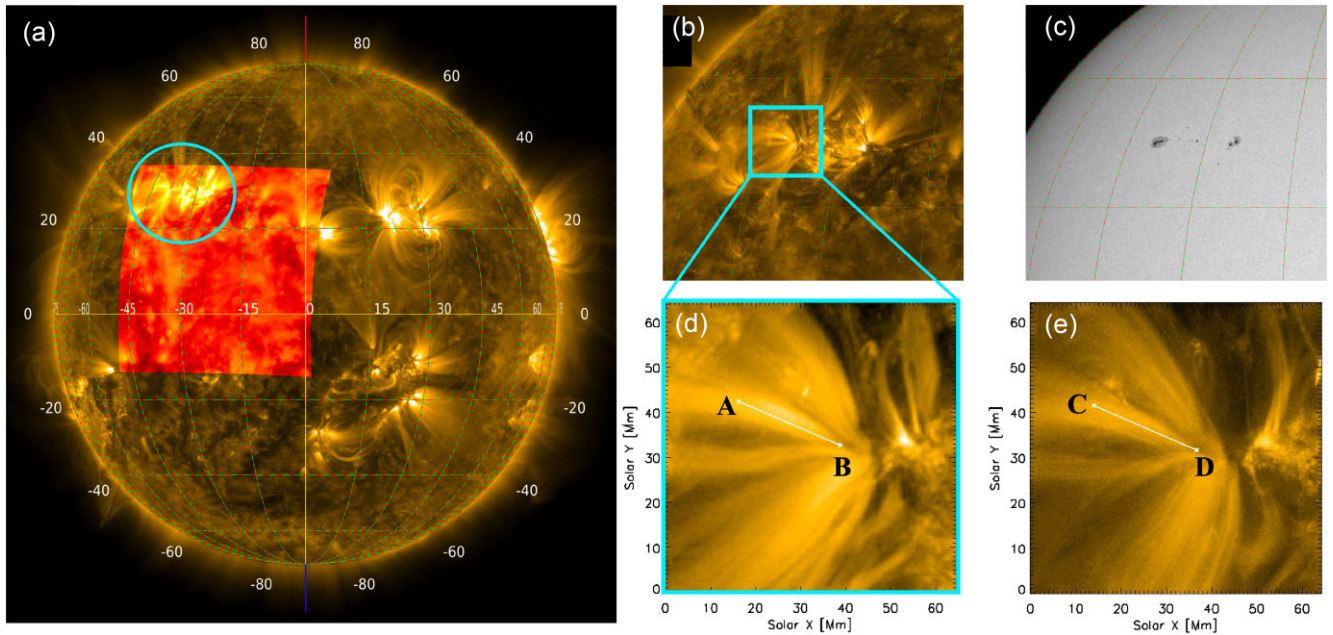


Figure 2. Panel (a): Solar disc as seen by SDO/AIA, the red region shows the SoLO/EUI-HRIEUV FoV. The blue oval indicates AR 12941, of interest. Panel (b): AR 12941 in more detail observed by AIA. Panel (c) HMI continuum for the same view as panel (b), shows the sunspots that the coronal fan is anchored in. Panels (d) and (e): active region viewed from AIA and HRIEUV, respectively, with the slit used for the time distance analysis in white.

(2011); Krishna Prasad et al. (2018) used spectral observations of slow waves to estimate the polytropic index.

This paper presents the first simultaneous detection of propagating slow waves with the Atmospheric Imaging Assembly (AIA; Lemen et al. 2012) on the Solar Dynamics Observatory (SDO) and the high-resolution Extreme Ultraviolet Imager (EUI; Rochus et al. 2020) on the Solar Orbiter (SoLO). We investigate the damping length of each wave with AIA and HRIEUV (EUI’s High Resolution Imager at the 174 Å wavelength) and estimate the inclination angle between the direction of the wave propagation and the AIA and HRIEUV line-of-sight (LoS). In Section 2, we describe the observations and data processing. In Section 3, the data analysis and the results obtained are presented. Discussion and conclusions are in Section 4.

2 OBSERVATIONS AND DATA PROCESSING

Slow waves are observed propagating along a coronal fan anchored in the east sunspot in β -Hale class active region (AR) 12941, on February 7th 2022 at 12:45–14:15 UT. The waves emerge near the centre of the fan and travel upwards parallel to the loops within the fan. This event was simultaneously captured by AIA and HRIEUV with a LoS separation of 19°, see Fig. 1.

AIA is positioned in a geo-synchronous orbit and observes the full solar disc with a time cadence of 12 s and a pixel size of 0.6 arcsec. This gives a plate scale of 0.429 Mm pixel⁻¹. Among six EUV passbands of AIA, the 171 Å is selected as it shows the high-contrast features in the corona and as it is the most similar to the 174 Å passband of HRIEUV. For the duration of the event, EUI is at a distance of 0.799 au from the Sun, and a pixel size of 0.492 arcsec in HRIEUV images gives a corresponding plate scale of 0.285 Mm pixel⁻¹. The HRIEUV 174 Å images have a cadence of 5 s for the duration of the event. The field of view (FoV) of AIA for this event is shown in Fig. 2(a). The red region is the FoV of HRIEUV, and AR 12941 is indicated with the turquoise oval. Panel (b) shows the active region in more detail, and panel (c) shows the SDO Helioseismic and Magnetic Imager (HMI) continuum for the

active region. There are three sunspots anchoring the coronal fans. The cropped regions of interest viewed from AIA and HRIEUV are shown in panels (d–e), respectively.

AIA Level 1 data is downloaded from JSOC¹ and corrected for solar rotation. The HRIEUV data downloaded² is Level 2, which is calibrated. Then data is internally aligned using cross-correlation techniques as described in Zhong et al. (2022) and Chitta et al. (2022) to correct for the Sun’s rotation and spacecraft jitters. The observations are then coaligned in time to correct the difference in light travel time to AIA and HRIEUV of 94 s due to the different positions of the instruments in space.

These waves can be seen in both the original movies (see supplementary movies 1–2) as well as mean difference videos (see supplementary movies 3–4) produced by subtracting the mean of all frames from each individual frame in the observation.

3 DATA ANALYSIS AND RESULTS

3.1 Time–distance analysis

The time–distance analysis is conducted on mean difference images using a slit parallel to the direction of the wave propagation, see the white lines in Fig. 2(d–e) for AIA and HRIEUV, respectively. The bottom right point of the slit is positioned on a dark feature in both data sets. The resulting time–distance maps are shown in Fig. 3.

The waves can be seen through the entire duration of the 92-min data and are identified as tilted ridges at the base of the slit. Over thirty, almost continuous oscillation cycles are present. The oscillations can be seen in the AIA data up to approximately 6 Mm and past 10 Mm in the HRIEUV data. This is explored in more depth in Section 3.3.

¹<http://jsoc.stanford.edu/>

²https://www.astro.oma.be/doi/ROB-SIDC-Solo_EUI-DataRelease6.0_2023-01.html

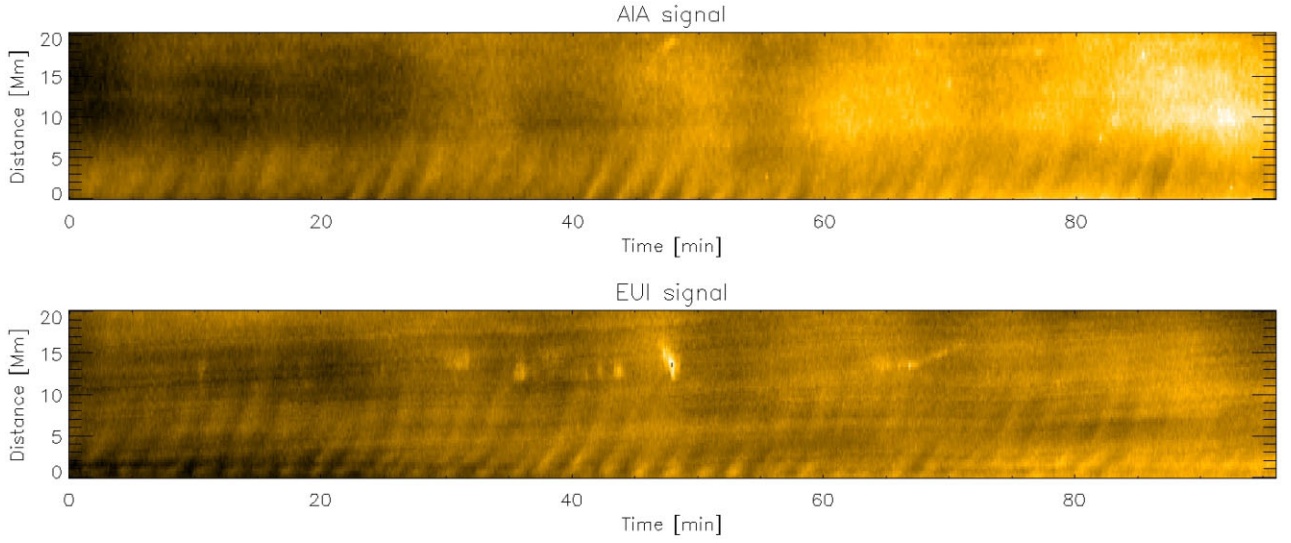


Figure 3. Time–distance maps produced from the slits identified in Fig. 2 for AIA (top) and HRIEUV (bottom) using mean-difference images. The HRIEUV signal intensity has been limited to a maximum intensity for visualization purposes. The propagating slow waves are seen as tilted ridges at the bottom of the plots.

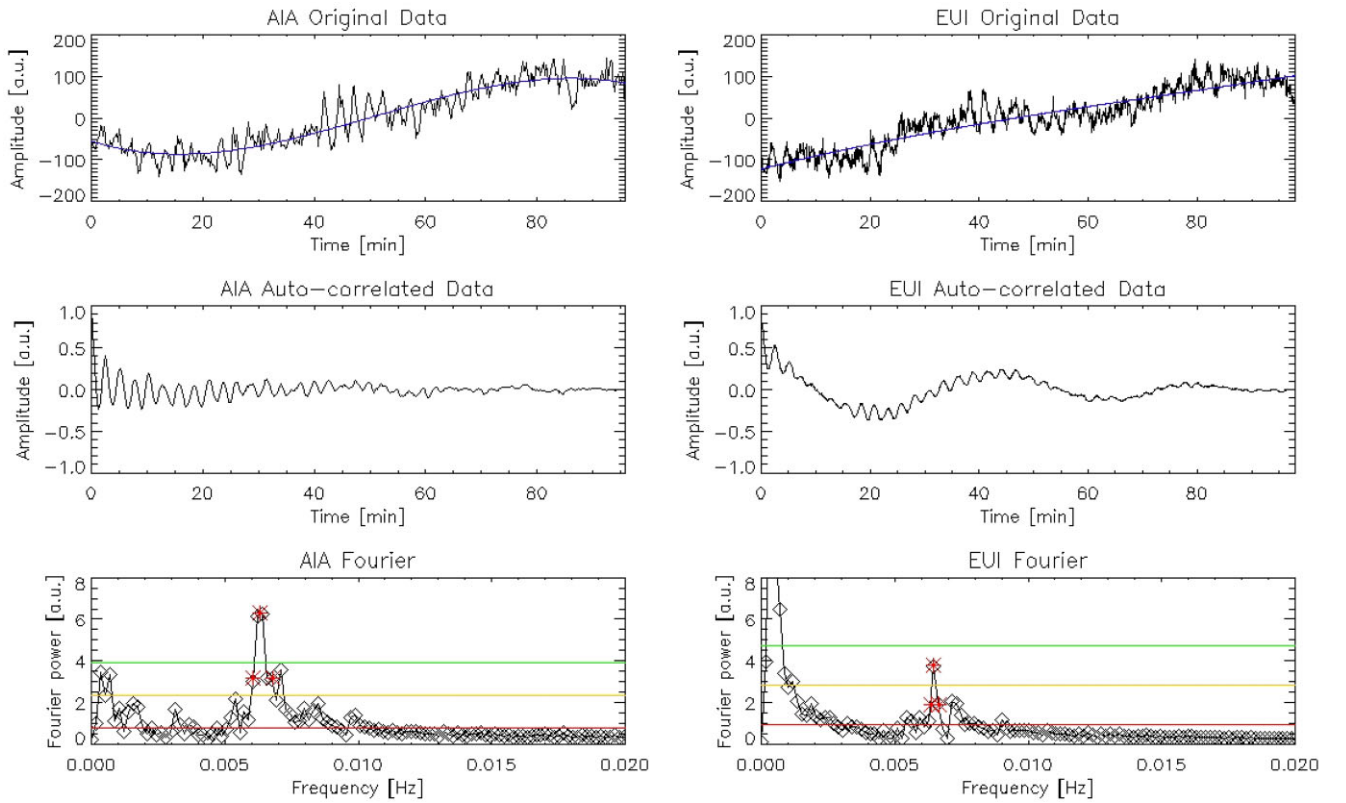


Figure 4. Determination of period of propagating slow wave detected by AIA (left) and HRIEUV (right). Top panels: original data taken from time distance maps at 1 Mm along the slit from Fig. 3. The blue line shows the trend fit using a third-order polynomial. Middle panels: autocorrelation functions of the detrended data from the top panels. Bottom panels: Fourier spectra of the autocorrelated data in middle panels. The horizontal red, orange, and green lines show 1, 3, and 5σ . The red points show the peak used to determine the period and the points for half maximum used to determine the error. The periods determined are $2.7^{+0.1}_{-0.2}$ and $2.6^{+0.1}_{-0.1}$ min for AIA and HRIEUV, respectively.

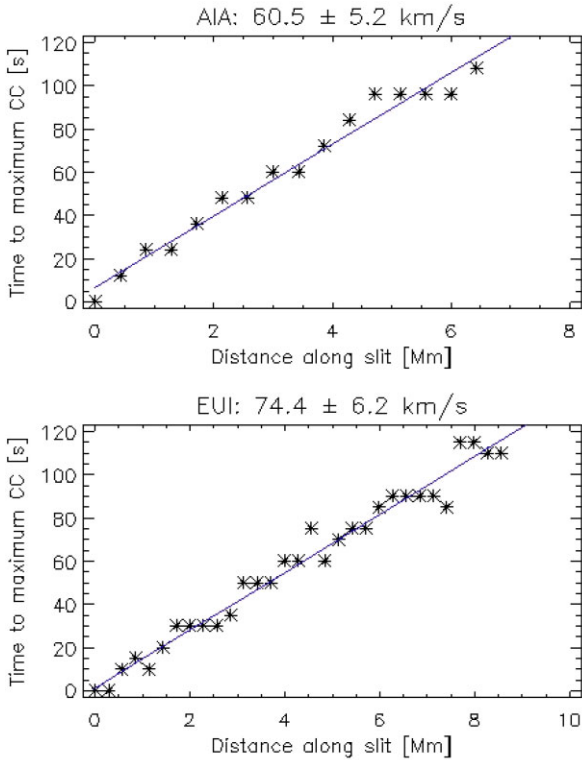


Figure 5. Time lag to reach maxima in the cross-correlation of intensity variation as a function of distance along the slit in AIA (top) and HRIEUV (bottom) time–distance data. The phase speed is given by the inverse of the gradient and the error is given by the corresponding 3σ in the least squares fit of the gradient. The calculated phase speeds and errors are given in the panels.

In the HRIEUV data between 30 and 50 min, bright regions in the time–distance map have been set to zero for visualization purposes. This brightening is present in the AIA and HRIEUV data. However, due to the difference in the LoS, the slit used for time–distance analysis in HRIEUV crosses this bright region but not AIA. In the AIA and HRIEUV data, we see a long-period brightening and dimming along the whole slit with a period around 20 min. Similar periodicities have been detected in the corona before, for example, in Ofman et al. (1997), Banerjee et al. (2001), Sych & Nakariakov (2008), and Pascoe et al. (2016). The physical interpretation of these long-period coronal oscillations is not yet understood. We also see a horizontal wavy pattern present in only HRIEUV data that is due to a sensor artefact (Gissot et al. (in prep)). These lines result from a discontinuity in the low and high gain pixels in the combined gain HRIEUV images. It is currently unavoidable and requires a solution in the future from the EUV team. For this study, as the period of such an artefact is much longer than the periodicity of interest, we can mitigate it by subtracting the trend in the time–distance data.

3.2 Determining wave parameters

The wave period is determined by selecting the time-varying intensity at 1 Mm along the slit, this is shown in the top panels of Fig. 4, for AIA (left) and HRIEUV (right). A third-order polynomial shown by the blue lines, is fitted and subtracted to remove the trend. The autocorrelation function is then calculated and is shown in the middle panels. Then the period is determined by selecting the peak in the

Fourier spectra for the autocorrelation data, shown in the bottom panels. The red stars show the peak period selected and the half maximum used to determine the errors. The red, orange, and green lines show the 1, 3, and 5σ values. The lower frequency peak in the HRIEUV data is ignored as it corresponds to the sensor artefact indicated earlier. The periods determined are $2.7^{+0.1}_{-0.2}$ and $2.6^{+0.1}_{-0.1}$ min for AIA and HRIEUV, respectively.

The projected phase speed is determined by finding the time to reach the maximum in a cross-correlation function between 0 Mm and each pixel along the slit (see Section 4.1.3 in Anfinogentov et al. 2022, for details). The time taken to reach a maximum as a function of the length along the slit is shown in Fig. 5. The inverse of the gradient gives the velocity, and the error is given by 3σ for the linear fit. The determined projected phase speeds are 60.5 ± 5.2 and 74.4 ± 6.2 km s⁻¹ for AIA and HRIEUV, respectively. The speed is a minimum of the phase speed as we can only see the component of velocity perpendicular to the LoS.

We can predict the inclination of the wave propagation direction by assuming that the actual phase speed coincides with the local sound speed c_s and using that c_s (km s⁻¹) $\approx 152\sqrt{T(\text{MK})}$, where T is the loop temperature in MK. The inclination from the LoS, θ , the actual phase speed c_s , and the observed projected speed v are connected as $c_s = v/\sin(\theta)$. The temperature T is estimated by finding the mean of the peak in the AIA and HRIEUV response functions. For AIA, the peak corresponds to 0.813 MK, and for HRIEUV, it is 0.955 MK, giving the mean value $T = 0.884$ MK and $c_s \approx 143$ km s⁻¹. The above relation can then be used to calculate the inclination of the wave propagation direction to the LoS (see Fig. 6). We obtain two solutions, $\theta_{\text{AIA}} = 25 \pm 2^\circ$ and $\theta_{\text{EUV}} = 31 \pm 3^\circ$ (the wave vector is directed towards the observer) or $\pi - \theta$, i.e. $\theta_{\text{AIA}} = 155 \pm 2^\circ$ and $\theta_{\text{EUV}} = 149 \pm 3^\circ$ (the wave vector is directed away from the observer). The calculated parameters are given in Table 1.

3.3 Amplitude along slit

In order to explore the 2.6-min oscillations in more detail, we subtract the trend determined by smoothing with a 200-s window for each pixel along the slit. The resulting map is shown in Figs 7(a)–(b). Then, to analyse the evolution of the wave amplitude along the slit, we focus on a cropped region of the smoothed data indicated by the turquoise box in the top two panels, which ensures that we do not include the region of the bright spot that will increase the amplitude for reasons other than the slow waves of interest. This region is filtered using a Gaussian filter centred on the peak in the Fourier spectrum between 2.5 and 3.5 min, with a width of 0.001 Hz. The filtered time–distance data is shown in panels (c) and (d) for AIA and HRIEUV, respectively. The wave amplitude is then determined by finding the difference between consecutive maxima and minima for each oscillation cycle in the data. Plots (e–f) show the wave amplitude as a function of distance along the slit. For each distance along the slit, the error in the mean amplitude is given by the standard deviation of the instantaneous amplitude at this distance. The mean of the amplitude errors for all distances gives the error in the initial amplitude. This error is propagated by determining where the amplitude decreases by a factor of e (the e -folding length) for the initial amplitude plus the mean error and the e -folding length for the initial amplitude minus the mean error. This results in an asymmetric error due to the non-linear decay pattern, as shown by the grey-shaded area in Figs 7(e)–(f). Hence, we determine the decay lengths to be $6.9^{+1.3}_{-0.8}$ Mm for AIA and $12.8^{+1.1}_{-1.7}$ Mm for HRIEUV. These values are reflected in the filtered data when observed manually by eye.

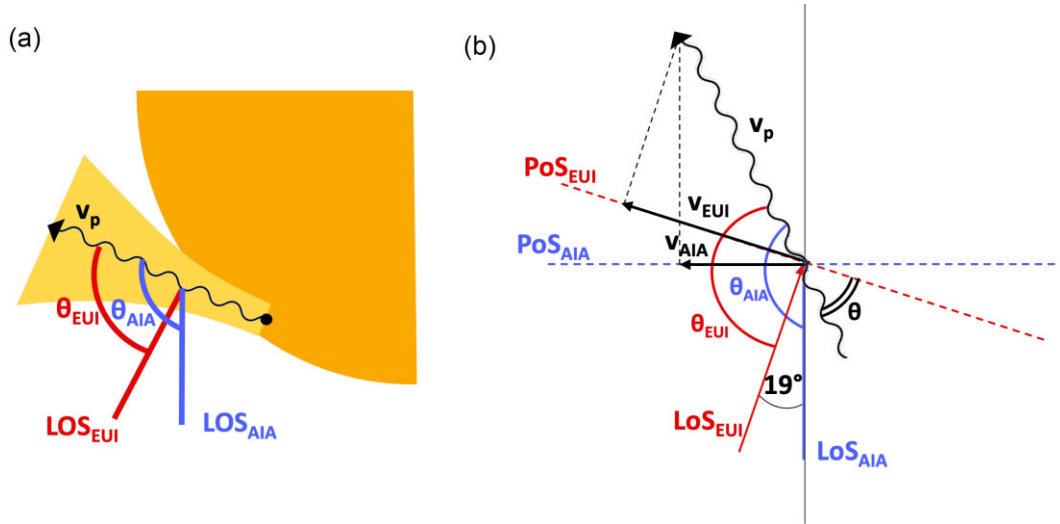


Figure 6. a) A sketch demonstrating the estimated angles calculated in Table 1 from a top-down view of the Sun. The light yellow funnel-like structure represents the loop fan of study. b) A schematic plan view of the observed wave and orientation of AIA and EUV. v_p is the wave phase speed approximated by the sound speed, v_{AIA} (v_{EUI}) is the projected wave speed observed by AIA (EUV).

Table 1. Parameters of the propagating slow wave, determined with the use of AIA and HRI, for the assumed loop temperature $T = 0.884$ MK (estimated as the mean of the peak temperatures in the AIA and HRIEUV response functions).

Wave Parameter	AIA	HRIEUV
Projected phase speed (km s^{-1})	60.5 ± 5.2	74.4 ± 6.2
Predicted phase speed (km s^{-1})	143	143
Inclination to line of sight ($^\circ$)	25 ± 2 or 155 ± 2	31 ± 3 or 149 ± 3

3.4 Cross-correlation

We have identified periods for the waves that agree within the error bars, with similar speeds accounting for the difference in the inclination from the LoS. However, we observe substantially different decay lengths with each instrument. To ensure that we are observing the same event with both instruments, we look at the cross-correlation coefficient of the data sets. First, we compute the autocorrelation function of the time–distance data for each distance along the slit for both the AIA and HRIEUV data. Then we calculate the cross-correlation coefficient (R) between the AIA and HRIEUV data for each pixel along the slit. Fig. 8 shows the dependence of R on the distance along the slit. We see a high correlation with $R \approx 0.7$ – 0.8 between two data sets for the lower distances along the slit, which drops below $R \approx 0.6$ around 5 Mm along the slit. The latter value is consistent with the e -folding distance of the slow wave amplitude in AIA observations, estimated in Section 3.3.

4 DISCUSSION AND CONCLUSIONS

We present the first simultaneous observation of slow waves with SDO/AIA and SoO/EUV, with two non-parallel LoS separated by 19° . Previous works with simultaneous observations have confirmed the natural origin of propagating EUV disturbances as slow waves with several combinations of instruments (e.g. TRACE & EIT (Robbrecht et al. 2001), TRACE & CDS (Marsh et al. 2003), and STEREO A & STEREO B (Marsh, Walsh & Plunkett

2009)). However, a detailed comparison of the wave properties observed with multiple instruments has not been performed since Marsh, De Moortel & Walsh (2011) determined the decay length using STEREO A and STEREO B data. Their estimation of the decay length is consistent with our results within the error bars.

Here, we have developed on previous works by capitalizing on a new combination of instruments with AIA and HRIEUV that will be particularly useful in the future due to the high spatial and temporal resolution of HRIEUV, and almost continuous observations of AIA. The main findings of our study can be summarized as follows:

(i) Oscillation periods of $2.7_{-0.2}^{+0.1}$ and $2.6_{-0.1}^{+0.1}$ min are detected for AIA and HRIEUV, respectively. These periods agree within their error bars, and suggest that both instruments observe the same wave. Previous empirical studies have demonstrated that coronal loops and fans anchored in sunspots, as the loop configuration is here, see slow waves with periods of approximately 3 min. Our observation is in agreement with this previous empirical result.

(ii) We calculate cross-correlation coefficients for each distance along the slit used for time–distance analysis. These coefficients are about 0.8 for the distances along this slit, where the slow wave is detected by both instruments. It is improbable that such a high correlation could be produced by chance. In particular, the Fisher randomization test performed in Kolotkov et al. (2021) showed that the correlation between two data sets after random permutations can appear above 0.8 in less than 1 percent of all cases considered. Hence, we can confidently claim that AIA and HRIEUV are observing the same event. The coefficient drops below 0.6 around 5 Mm along the slit, where the AIA oscillatory signal degrades.

(iii) We calculate the projected slow wave phase speeds of 60.5 ± 5.2 and 74.4 ± 6.2 km s^{-1} for AIA and HRIEUV, respectively. In addition to the projection effect caused by different LoS, the measured speeds may also differ due to the fine structuring of the coronal fan. Different LoS could be viewing different strands of the fan at different temperatures, resulting in different actual propagation

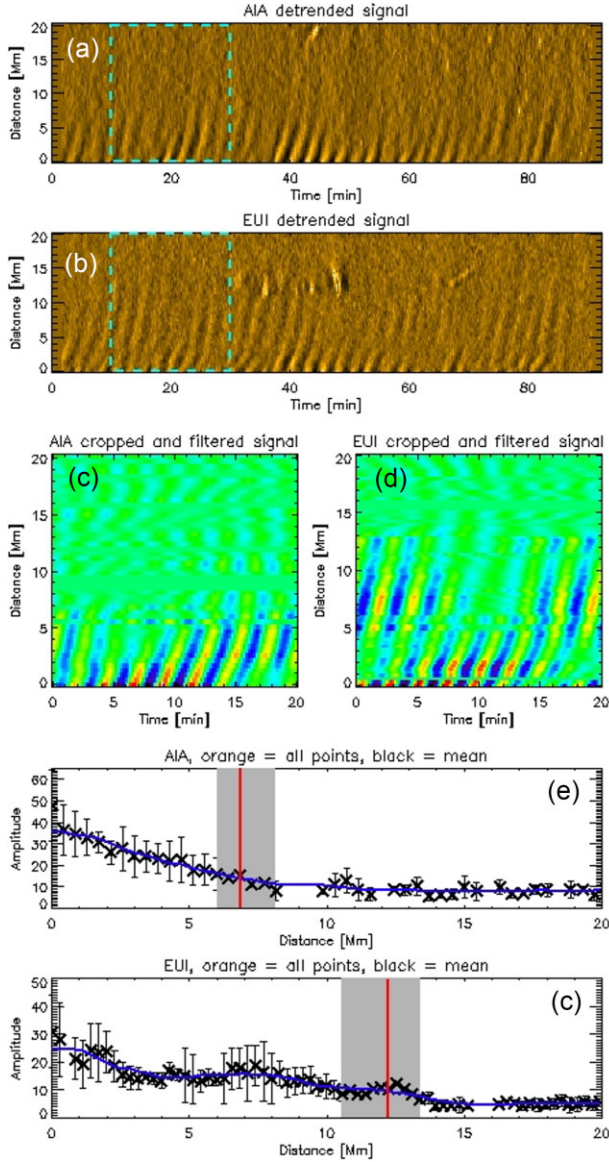


Figure 7. Panels (a–b): AIA (a) and HRIEUV (b) time–distance maps, detrended by subtracting smoothed data with a window of 200 s. The regions indicated by the turquoise box are cropped and then filtered using a Gaussian filter centred on the maximum frequency between 2.5 and 3.5 min in the Fourier spectrum, with a width of 0.001 Hz. The resulting map is shown in Panels (c) and (d) for AIA and HRIEUV, respectively. The colour scheme is changed for visualization. The intensity in panels (c–d) is normalized to the corresponding maximum values. Panels (e–f) show the wave amplitude as a function of distance along the slit. Black crosses indicate the mean value of the amplitude for each pixel along the slit and the error bars are determined by the standard deviation in the individual amplitudes. The blue curve is the smoothed mean points. The red vertical line indicates where the initial amplitude has decreased by a factor of e and the grey shaded region indicates the error in the decay length determined by propagating the mean error in the amplitudes. The decay length is $6.9^{+1.3}_{-0.8}$ Mm for AIA and $12.8^{+1.1}_{-1.7}$ Mm for HRIEUV.

speeds. Likewise, AIA and HRIEUV may capture subresolution plasma threads with different temperatures due to the difference in their response functions. Despite the peak temperatures being similar, the response function of HRIEUV is broader (e.g. Chen et al. 2021), which may also result in observing different propagation speeds. The

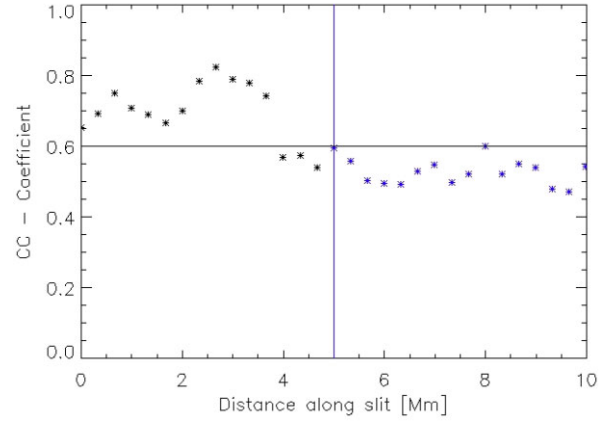


Figure 8. Cross-correlation coefficients (R) between oscillation signals extracted in AIA and HRIEUV time–distance data as a function of distance along slit. The vertical line marks the location where R is lower than 0.6.

assessment of the relative importance of these effects would require dedicated forward modelling work, which could be addressed in the future.

(iv) We estimate the angle of inclination of the wave vector from the LoS (see Fig. 6) by assuming that the temperature of the observed plasma fan is the mean value of the peaks in the instrument response functions. The calculated values are $25 \pm 2^\circ$ or $155 \pm 2^\circ$ relative to the AIA LoS and $31 \pm 3^\circ$ or $149 \pm 3^\circ$ relative to the HRIEUV LoS. Due to the physical orientation of the instruments and the fan pointing eastward in the images from both instruments, we note that the angle from the line of sight with AIA must be larger than that with HRIEUV. Hence, we conclude that the angles from the lines of sight must be $\theta_{\text{AIA}} = 155 \pm 2^\circ$ and $\theta_{\text{EUI}} = 149 \pm 3^\circ$ and that the wave vector is directed away from the observer. See Fig. 6b) for a schematic plan view of the wave and instrument orientation. Since Marsh, Walsh & Plunkett (2009), our study became the first to measure the slow wave propagation direction using two vantage point observations. However, the exact temperature of the observed plasma could be a range of values within the instrument response functions. A more rigorous method of determining the temperature, such as differential emission measure analysis (see e.g. Krishna Prasad et al. 2018; Krishna Prasad, Jess & Van Doorsselaere 2019) would provide a better estimate of the inclination of the wave. Another interesting next step could be to compare this calculated angle to the magnetic field extrapolation for this active region. This is because slow waves in the low- β coronal plasma propagate almost parallel to magnetic field lines. Hence, the wave vector should represent the local direction of the magnetic field. Simultaneous observations of slow waves with AIA and HRIEUV from two different vantage points open up interesting opportunities for these implications.

(v) The e -folding length of the slow wave as seen by AIA and HRIEUV are found to be substantially different, $6.9^{+1.3}_{-0.8}$ and $12.8^{+1.1}_{-1.7}$ Mm, respectively. The geometry shown in Fig. 6b) is identical for the projected phase speed and the projected decay length. We use $\theta = \theta_{\text{EUI}} - 90^\circ$, the angle between the wave vector and EUI PoS, as a reference angle. Then we can write $\lambda_{\text{EUI}} = \lambda \cos(\theta)$ and $\lambda_{\text{AIA}} = \lambda \cos(\theta + 19^\circ)$, where λ is the absolute decay length and λ_{AIA} and λ_{EUI} are the projected decay lengths seen with AIA and EUI, respectively.

If the only factor impacting both the speed and decay length is projection effects, the ratio of each with instruments should be equal, that is:

$$\frac{\lambda_{\text{AIA}}}{\lambda_{\text{EUV}}} = \frac{v_{\text{AIA}}}{v_{\text{EUV}}}. \quad (1)$$

However, we see that $\frac{\lambda_{\text{AIA}}}{\lambda_{\text{EUV}}} \approx 0.5$ and $\frac{v_{\text{AIA}}}{v_{\text{EUV}}} \approx 0.8$. The calculations for the projected phase speed are more reliable and so there must be other factors that influence the decay length of the waves. This indicates, for the first time, that the observed spatial damping of propagating slow waves in the solar corona is instrument dependent. The reason for this difference is currently unknown and should be explored in more depth. A combination of effects such as different response functions of AIA and HRIEUV, different viewing angles and multi-stranded structure of the wave-hosting coronal fan; different background plasma dynamics and integration along the LoS; or an apparent damping of slow-waves by the effect of phase mixing caused by a non-uniform transverse temperature profile (Voitenko et al. 2005) as discussed in Fedenev et al. (submitted) and Van Doorselaere et al. (in preparation) can potentially lead to this disparity. However, a dedicated follow-up forward modelling study is needed to address this question properly, using our work as an observational reference point for comparison.

Thus, the use of two independent EUV imagers with non-parallel LoS has clear advantages for studying slow magnetoacoustic waves in the corona. Moreover, with an improved spatial (up to $0.1 \text{ Mm pixel}^{-1}$ plate scale at perihelion) and temporal resolution (up to 2 s cadence), HRIEUV will allow the conduction of studies on slow magnetoacoustic waves that have not yet been possible. Such future studies may include investigating the evolution of the wave shape with height and damping length of higher wave harmonics as a function of the period.

ACKNOWLEDGEMENTS

The following fundings are gratefully acknowledged: China Scholarship Council-University of Warwick joint scholarship (SZ), the EU Guest Investigatorship (SZ and VMN.), the STFC consolidated grant ST/X000915/1 (D.Y.K.), the Latvian Council of Science Project No. lzp2022/1-0017 (DYK. and VMN.). The data is used courtesy of the SDO/AIA, SDO/HMI team, and EUV team. The EUV instrument was built by CSL, IAS, MPS, MSSL/UCL, PMOD/WRC, ROB, LCF/IO with funding from the Belgian Federal Science Policy Office (BEL-SPO/PRODEX PEA 4000134088, 4000112292, 4000117262, and 4000134474), the Centre National d'Etudes Spatiales (CNES); the UK Space Agency (UKSA); the Bundesministerium für Wirtschaft und Energie (BMWi) through the Deutsches Zentrum für Luft-und Raumfahrt (DLR) and the Swiss Space Office (SSO).

DATA AVAILABILITY

In this paper, we analysed data using the Interactive Data Language (IDL), SolarSoftWare (SSW; Freeland & Handy 1998) package. The EUV data are available at DOI: <https://doi.org/10.24414/z818-4163>. The AIA and HMI data are available at <http://jsoc.stanford.edu/>.

REFERENCES

- Anfinogentov S. A. et al., 2022, *Space Sci. Rev.*, 218, 9
 Arregui I., Kolotkov D. Y., Nakariakov V. M., 2023, *A&A*, 677, A23
 Banerjee D., O'Shea E., Doyle J. G., Goossens M., 2001, *A&A*, 377, 691

- Banerjee D. et al., 2021, *Space Sci. Rev.*, 217, 76
 Berghmans D., Clette F., 1999, *Sol. Phys.*, 186, 207
 Botha G. J. J., Arber T. D., Nakariakov V. M., Zhugzhda Y. D., 2011, *ApJ*, 728, 84
 Chen Y., Przybylski D., Peter H., Tian H., Auchère F., Berghmans D., 2021, *A&A*, 656, L7
 Chitta L. P. et al., 2022, *A&A*, 667, A166
 De Moortel I., 2006, *Phil. T. R. Soc. Lond. Ser. A*, 364, 461
 de Moortel I., 2009, *Space Sci. Rev.*, 149, 65
 De Moortel I., Hood A. W., 2003, *A&A*, 408, 755
 De Moortel I., Hood A. W., 2004, *A&A*, 415, 705
 De Moortel I., Ireland J., Walsh R. W., 2000, *A&A*, 355, L23
 De Moortel I., Ireland J., Walsh R. W., Hood A. W., 2002a, *Sol. Phys.*, 209, 61
 De Moortel I., Hood A. W., Ireland J., Walsh R. W., 2002b, *Sol. Phys.*, 209, 89
 DeForest C. E., Gurman J. B., 1998, *ApJ*, 501, L217
 Freeland S. L., Handy B. N., 1998, *Sol. Phys.*, 182, 497
 Kiddie G., De Moortel I., Del Zanna G., McIntosh S. W., Whittaker I., 2012, *Sol. Phys.*, 279, 427
 King D. B., Nakariakov V. M., Deluca E. E., Golub L., McClements K. G., 2003, *A&A*, 404, L1
 Kolotkov D. Y., 2022, *Front. Astron. Space Sci.*, 9, 402
 Kolotkov D. Y., Nakariakov V. M., 2022, *MNRAS*, 514, L51
 Kolotkov D. Y., Nakariakov V. M., Zavershinskii D. I., 2019, *A&A*, 628, A133
 Kolotkov D. Y., Duckenfield T. J., Nakariakov V. M., 2020, *A&A*, 644, A33
 Kolotkov D. Y., Nakariakov V. M., Holt R., Kuznetsov A. A., 2021, *ApJ*, 923, L33
 Kolotkov D. Y., Nakariakov V. M., Fihosy J. B., 2023, *Physics*, 5, 193
 Krishna Prasad S., Banerjee D., Singh J., 2012a, *Sol. Phys.*, 281, 67
 Krishna Prasad S., Banerjee D., Van Doorselaere T., Singh J., 2012b, *A&A*, 546, A50
 Krishna Prasad S., Banerjee D., Van Doorselaere T., 2014, *ApJ*, 789, 118
 Krishna Prasad S., Jess D. B., Klimchuk J. A., Banerjee D., 2017, *ApJ*, 834, 103
 Krishna Prasad S., Raes J. O., Van Doorselaere T., Magyar N., Jess D. B., 2018, *ApJ*, 868, 149
 Krishna Prasad S., Jess D. B., Van Doorselaere T., 2019, *Front. Astron. Space Sci.*, 6, 57
 Lemen J. R. et al., 2012, *Sol. Phys.*, 275, 17
 Mandal S., Magyar N., Yuan D., Van Doorselaere T., Banerjee D., 2016, *ApJ*, 820, 13
 Mandal S., Krishna Prasad S., Banerjee D., 2018, *ApJ*, 853, 134
 Marsh M. S., Walsh R. W., De Moortel I., Ireland J., 2003, *A&A*, 404, L37
 Marsh M. S., Walsh R. W., Plunkett S., 2009, *ApJ*, 697, 1674
 Marsh M. S., De Moortel I., Walsh R. W., 2011, *ApJ*, 734, 81
 Morgan H., Hutton J., 2018, *ApJ*, 853, 145
 Morgan H., Habbal S. R., Li X., 2004, *ApJ*, 605, 521
 Nakariakov V. M., 2006, *Phil. T. R. Soc. Lond. Ser. A*, 364, 473
 Nakariakov V. M., Kolotkov D. Y., 2020, *ARA&A*, 58, 441
 Nakariakov V. M., Verwichte E., Berghmans D., Robbrecht E., 2000, *A&A*, 362, 1151
 Ofman L., Romoli M., Poletto G., Noci G., Kohl J. L., 1997, *ApJ*, 491, L111
 Owen N. R., De Moortel I., Hood A. W., 2009, *A&A*, 494, 339
 Pascoe D. J., Goddard C. R., Nisticò G., Anfinogentov S., Nakariakov V. M., 2016, *A&A*, 585, L6
 Prasad A., Srivastava A. K., Wang T., 2021, *Sol. Phys.*, 296, 105
 Reale F., Testa P., Petralia A., Kolotkov D. Y., 2019, *ApJ*, 884, 131
 Robbrecht E., Verwichte E., Berghmans D., Hochedez J. F., Poedts S., Nakariakov V. M., 2001, *A&A*, 370, 591
 Roberts B., Webb A. R., 1978, *Sol. Phys.*, 56, 5
 Rochus P. et al., 2020, *A&A*, 642, A8

- Stenborg G., Marsch E., Vourlidas A., Howard R., Baldwin K., 2011, *A&A*, 526, A58
- Sych R. A., Nakariakov V. M., 2008, *Sol. Phys.*, 248, 395
- Tsiklauri D., Nakariakov V. M., 2001, *A&A*, 379, 1106
- Uritsky V. M., Davila J. M., Viall N. M., Ofman L., 2013, *ApJ*, 778, 26
- Van Doorselaere T., Wardle N., Del Zanna G., Jansari K., Verwichte E., Nakariakov V. M., 2011, *ApJ*, 727, L32
- Verwichte E., Marsh M., Foullon C., Van Doorselaere T., De Moortel I., Hood A. W., Nakariakov V. M., 2010, *ApJ*, 724, L194
- Voitenko Y., Andries J., Copil P. D., Goossens M., 2005, *A&A*, 437, L47
- Wang T. J., Ofman L., Davila J. M., Mariska J. T., 2009a, *A&A*, 503, L25
- Wang T. J., Ofman L., Davila J. M., 2009b, *ApJ*, 696, 1448
- Wang T., Ofman L., Yuan D., Reale F., Kolotkov D. Y., Srivastava A. K., 2021, *Space Sci. Rev.*, 217, 34

- Zhong S., Nakariakov V. M., Kolotkov D. Y., Verbeeck C., Berghmans D., 2022, *MNRAS*, 516, 5989
- Zhugzhda Y. D., 1996, *Phys. Plasmas*, 3, 10

SUPPORTING INFORMATION

Supplementary data are available at *MNRAS* online.

Please note: Oxford University Press is not responsible for the content or functionality of any supporting materials supplied by the authors. Any queries (other than missing material) should be directed to the corresponding author for the article.

This paper has been typeset from a $\text{\TeX}/\text{\LaTeX}$ file prepared by the author.